中国激光

石英晶体椭偏测量中的穆勒矩阵模型

赵宇[1,2], 张灵浩[1,2], 曾爱军[1,2*], 黄惠杰[2], Sergey Avakaw[3]

[1]中国科学院上海光学精密机械研究所信息光学与光电技术实验室, 上海 201800;

[2]中国科学院大学材料科学与光电工程中心, 北京 100049;

[3]白俄罗斯共和国开放式股份公司“精密电子机械制造设计局-光学机械设备”, 白俄罗斯 明斯克 220033

摘要 石英晶体是一种重要的双折射材料,广泛应用于光学相关领域。石英晶体在宽光谱下的参数测量通常使用椭圆偏振法,但现有的椭偏测量仪器往往假定晶体的光轴与测量光路对准,从而引入测量误差,这一问题在紫外波段尤为显著。为此提出了一种采用椭圆偏振法精确测量石英晶体参数的穆勒矩阵模型,运用坐标变换和Berreman 4×4矩阵理论建立石英晶体参数与穆勒矩阵的关联,通过拟合计算可以得到晶体的厚度、光轴欧拉角和相位延迟量。实验结果显示,拟合得到的穆勒矩阵与测量结果高度一致,模型拟合的均方根误差<5,拟合厚度的相对误差<1%,拟合的欧拉角与测量结果吻合。该模型包含的信息丰富,拟合准确,对椭圆偏振法测量各向异性材料的精确参数具有重要参考价值。

关键词 测量; 椭偏技术; 石英晶体; 介电张量; 相位延迟量; 欧拉角

中图分类号 TN247; O436.3　　**文献标志码** A　　**DOI:** 10.3788/CJL221577

1 引　　言

石英晶体是一种常见的双折射材料,常常用来制作波片等偏振器件。采用石英晶体制作的波片广泛应用于光纤通信[1]、偏振成像探测[2]、生物医学[3]、微纳加工[4]、光学精密测量[5-6]等领域。石英晶体波片的两个主要光学参数是相位延迟量和快轴方位角。由于制造工艺、使用环境等因素的影响,这两个实际参数会偏离理论值,故在使用之前通常需要对其光学参数进行精密测量。

对于石英晶体波片,测量其相位延迟量的方法包括激光分频法[7]、外差干涉法[8-9]、光弹调制法[10]、旋转消光法[11]、椭圆偏振法[12-13]等。激光分频法是将待测波片插入激光腔中进行分频,并分析频差与相位延迟量的关系来得到待测波片的相位延迟量,但该方法无法测量快轴方位角,且只能在单一波长下测量。外差干涉法可以同时获取波片在某个波长下的相位延迟量和快轴方位角,但操作繁琐且测量速度慢,测量结果易受环境干扰。光弹调制法可以精确测量1/4波片在特定波长下的相位延迟量,但需要提前确定快轴方位角。旋转消光法通过旋转偏振元件来测量相位延迟量,可以实现宽光谱范围测量,但不可避免地会受到光强波动的影响,测量精度受限。椭圆偏振法近年来广泛应用于薄膜参数和集成电路制造的检测,具有非破坏性、高精度和高灵敏性等优点。利用椭圆偏振法的椭偏参数进行数据反演,也可以获得波片的相位延迟量和快轴方位角,特别是可以实现宽光谱范围内不同波长下的相位延迟量和快轴方位角的测量。

椭圆偏振法的测量准确性高度依赖于拟合模型,往往通过穆勒算法和广义椭偏参数计算待测参数。通常的拟合模型默认待测晶体“正确”放置于样品台,即晶体的光轴与测量坐标系对准,实际上受样品制作的加工精度和在样品台上的放置误差的影响,晶体的光轴与测量光路不能严格重合,将引入测量误差,特别是在紫外波段下,问题将更为明显。针对这一问题,本文利用双旋转补偿器型穆勒矩阵椭偏仪对石英晶体进行测量,提出了一种基于坐标变换和Berreman 4×4矩阵理论的穆勒矩阵模型。模型考虑了晶体坐标系与测量坐标系方向不一致的情况,可以快速精准地拟合得到多个参数,不仅可以得到相位延迟量,还可以得到晶体的光轴方向和厚度。

2 原理与方法

在各向异性材料的分析中,常使用Berreman 4×4矩阵理论[14]的数据分析法对其光学特性进行精确计算和分析研究。Schubert等[15-16]把这个方法应用到各向异性材料的广义椭偏数据计算之中。我们应用该理论提出穆勒矩阵模型。

收稿日期: 2022-12-30; **修回日期:** 2023-02-13; **录用日期:** 2023-02-27; **网络首发日期:** 2023-03-09

基金项目: 上海市集成电路科技支撑专项(20501110600)、上海市政府间科技合作计划(20500711300)

通信作者: *aijunzeng@siom.ac.cn

在晶体坐标系(a,b,c)中，石英晶体的介电张量$\boldsymbol{\varepsilon}$表示为

$$\boldsymbol{\varepsilon}=\begin{pmatrix}\varepsilon_a & 0 & 0\\ 0 & \varepsilon_b & 0\\ 0 & 0 & \varepsilon_c\end{pmatrix}, \tag{1}$$

式中：ε_a、ε_b、ε_c为晶体的主介电常数。

以穆勒矩阵椭偏仪的测量系统作为测量坐标系(x,y,z)，其中测量系统的水平通光轴为z轴，如图1所示。考虑石英晶体的主轴方向和测量坐标系不一致的情况，可把晶体坐标系(a,b,c)变换到测量坐标系(x,y,z)。坐标变换涉及到三个欧拉角，即ϕ_{E}、θ_{E}、ψ_{E}。首先，a-b平面绕c轴旋转角度ϕ_{E}，得到中间坐标系C_1；然后绕坐标系C_1的a_1轴旋转角度θ_{E}，形成中间坐标系C_2；最后绕坐标系C_2的c_2轴旋转角度ψ_{E}，变换为坐标系(x,y,z)。

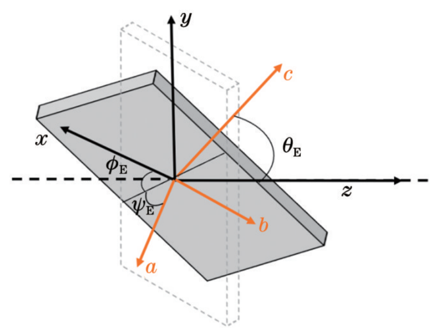

图1 晶体坐标系、测量坐标系与欧拉角

Fig. 1 Crystal coordinate system, measurement coordinate system and Euler angles

经过坐标变换之后，测量坐标系中的介电张量可以通过旋转矩阵$\boldsymbol{A}$来表达：

$$\boldsymbol{\varepsilon}_{\mathrm{lab}}=\begin{pmatrix}\varepsilon_{xx} & \varepsilon_{xy} & \varepsilon_{xz}\\ \varepsilon_{yx} & \varepsilon_{yy} & \varepsilon_{yz}\\ \varepsilon_{zx} & \varepsilon_{zy} & \varepsilon_{zz}\end{pmatrix}=\boldsymbol{A}^{\mathrm{T}}\begin{pmatrix}\varepsilon_a & 0 & 0\\ 0 & \varepsilon_b & 0\\ 0 & 0 & \varepsilon_c\end{pmatrix}\boldsymbol{A}, \tag{2}$$

$$\boldsymbol{A}=\begin{bmatrix}\cos\phi_{\mathrm{E}}\cos\psi_{\mathrm{E}}-\sin\phi_{\mathrm{E}}\cos\theta_{\mathrm{E}}\sin\psi_{\mathrm{E}} & -\cos\phi_{\mathrm{E}}\sin\psi_{\mathrm{E}}-\sin\phi_{\mathrm{E}}\cos\theta_{\mathrm{E}}\cos\psi_{\mathrm{E}} & \sin\phi_{\mathrm{E}}\sin\theta_{\mathrm{E}}\\ \sin\phi_{\mathrm{E}}\cos\psi_{\mathrm{E}}+\cos\phi_{\mathrm{E}}\cos\theta_{\mathrm{E}}\sin\psi_{\mathrm{E}} & -\sin\phi_{\mathrm{E}}\sin\psi_{\mathrm{E}}+\cos\phi_{\mathrm{E}}\cos\theta_{\mathrm{E}}\cos\psi_{\mathrm{E}} & -\cos\phi_{\mathrm{E}}\sin\theta_{\mathrm{E}}\\ \sin\theta_{\mathrm{E}}\sin\psi_{\mathrm{E}} & \sin\theta_{\mathrm{E}}\cos\psi_{\mathrm{E}} & \cos\theta_{\mathrm{E}}\end{bmatrix}。 \tag{3}$$

由 Berreman 4×4 矩阵理论有方程[14,16-17]

$$\partial_z\left[E_x,E_y,H_x,H_y\right]^{\mathrm{T}}=\mathrm{i}\frac{\omega}{c}\boldsymbol{\Delta}\left[E_x,E_y,H_x,H_y\right]^{\mathrm{T}}, \tag{4}$$

式中：ω为圆频率；c为光速；$\boldsymbol{\Delta}$为方程的特征矩阵，表示为

$$\boldsymbol{\Delta}=\begin{bmatrix}-\sin\theta_{\mathrm{i}}\dfrac{\varepsilon_{zx}}{\varepsilon_{zz}} & -\sin\theta_{\mathrm{i}}\dfrac{\varepsilon_{zy}}{\varepsilon_{zz}} & 0 & 1-\dfrac{\sin^2\theta_{\mathrm{i}}}{\varepsilon_{zz}}\\ 0 & 0 & -1 & 0\\ \varepsilon_{yz}\dfrac{\varepsilon_{zx}}{\varepsilon_{zz}}-\varepsilon_{yx} & \sin^2\theta_{\mathrm{i}}-\varepsilon_{yy}+\varepsilon_{yz}\dfrac{\varepsilon_{zy}}{\varepsilon_{zz}} & 0 & \sin\theta_{\mathrm{i}}\dfrac{\varepsilon_{yz}}{\varepsilon_{zz}}\\ \varepsilon_{xx}-\varepsilon_{xz}\dfrac{\varepsilon_{zx}}{\varepsilon_{zz}} & \varepsilon_{xy}-\varepsilon_{xz}\dfrac{\varepsilon_{zy}}{\varepsilon_{zz}} & 0 & -\sin\theta_{\mathrm{i}}\dfrac{\varepsilon_{xz}}{\varepsilon_{zz}}\end{bmatrix}, \tag{5}$$

式中：θ_{i}为光束入射角。

特征矩阵包含了光束的入射角和介质的介电常数。

引入入射矩阵$\boldsymbol{L}_{\mathrm{i}}$、出射矩阵$\boldsymbol{L}_{\mathrm{t}}$、部分传输矩阵$\boldsymbol{T}_{\mathrm{p}}(-d)$和传输矩阵$\boldsymbol{T}$：

$$\boldsymbol{L}_{\mathrm{i}}\left[E_{\mathrm{is}},E_{\mathrm{rs}},E_{\mathrm{ip}},E_{\mathrm{rp}}\right]^{\mathrm{T}}=\left[E_x(0),E_y(0),H_x(0),H_y(0)\right]^{\mathrm{T}}, \tag{6}$$

$$\boldsymbol{L}_{\mathrm{t}}\left[E_{\mathrm{ts}},0,E_{\mathrm{tp}},0\right]^{\mathrm{T}}=\left[E_x(d),E_y(d),H_x(d),H_y(d)\right]^{\mathrm{T}}, \tag{7}$$

$$\boldsymbol{T}_{\mathrm{p}}(-d)=\exp\left[\mathrm{i}\frac{\omega}{c}\boldsymbol{\Delta}(-d)\right], \tag{8}$$

$$\boldsymbol{T}=\begin{bmatrix}T_{11} & T_{12} & T_{13} & T_{14}\\ T_{21} & T_{22} & T_{23} & T_{24}\\ T_{31} & T_{32} & T_{33} & T_{34}\\ T_{41} & T_{42} & T_{43} & T_{44}\end{bmatrix}=\boldsymbol{L}_{\mathrm{i}}^{-1}\boldsymbol{T}_{\mathrm{p}}(-d)\boldsymbol{L}_{\mathrm{t}}, \tag{9}$$

式中：下标i、t和r分别表示光的入射、透射和反射；d为各向异性介质的厚度；下标p和s分别表示p偏振光和s偏振光。传输矩阵$\boldsymbol{T}$为4×4矩阵，包含了光束的入射角、入射光的波长以及介质的介电常数、厚度和欧拉角等参数。

入射光和透射光的偏振态关系可通过如下所示的传输矩阵联系：

$$\left[E_{\mathrm{is}},E_{\mathrm{rs}},E_{\mathrm{ip}},E_{\mathrm{rp}}\right]^{\mathrm{T}}=\boldsymbol{T}\left[E_{\mathrm{ts}},0,E_{\mathrm{tp}},0\right]^{\mathrm{T}}。 \tag{10}$$

样品的透射琼斯矩阵可以通过传输矩阵的元素计算：

$$\boldsymbol{J}=\begin{bmatrix}t_{\mathrm{pp}} & t_{\mathrm{ps}}\\ t_{\mathrm{sp}} & t_{\mathrm{ss}}\end{bmatrix}, \tag{11}$$

$$t_{\mathrm{pp}}=\left(\frac{E_{\mathrm{tp}}}{E_{\mathrm{ip}}}\right)_{E_{\mathrm{is}}=0}=\frac{T_{11}}{T_{11}T_{33}-T_{13}T_{31}}, \tag{12}$$

$$t_{\mathrm{sp}}=\left(\frac{E_{\mathrm{ts}}}{E_{\mathrm{ip}}}\right)_{E_{\mathrm{is}}=0}=\frac{-T_{13}}{T_{11}T_{33}-T_{13}T_{31}}, \tag{13}$$

$$t_{\mathrm{ss}}=\left(\frac{E_{\mathrm{ts}}}{E_{\mathrm{is}}}\right)_{E_{\mathrm{ip}}=0}=\frac{T_{33}}{T_{11}T_{33}-T_{13}T_{31}}, \tag{14}$$

$$t_{\mathrm{ps}}=\left(\frac{E_{\mathrm{tp}}}{E_{\mathrm{is}}}\right)_{E_{\mathrm{ip}}=0}=\frac{-T_{31}}{T_{11}T_{33}-T_{13}T_{31}}, \tag{15}$$

式中：t_{pp}为p偏振光的透射系数；t_{ss}为s偏振光的透射系数；当偏振光经过各向异性材料时，p偏振光和s偏振光会发生交叉极化，用t_{ps}表示由p偏振光产生的s偏振光的透射系数，t_{sp}表示由s偏振光产生的p偏振光的透射系数[18]。

对于无退偏效应的过程，可以直接将琼斯矩阵转换为穆勒矩阵，以与椭偏仪测量的穆勒矩阵数据对应。转换方法如下：

$$\boldsymbol{M}=\begin{bmatrix}1&0&0&1\\1&0&0&-1\\0&1&1&0\\0&\mathrm{i}&-\mathrm{i}&0\end{bmatrix}(\boldsymbol{J}\otimes\boldsymbol{J}^{*})\begin{bmatrix}1&0&0&1\\1&0&0&-1\\0&1&1&0\\0&\mathrm{i}&-\mathrm{i}&0\end{bmatrix}^{-1},\tag{16}$$

式中：$\boldsymbol{J}^{*}$为$\boldsymbol{J}$的复共轭；$\otimes$表示克罗内克积[19]。

综上所述，通过坐标变换和Berreman 4×4矩阵理论建立了与晶体的光学厚度d、欧拉角($\phi_{\mathrm{E}},\theta_{\mathrm{E}},\psi_{\mathrm{E}}$)、介电张量$\varepsilon$等参数关联的穆勒矩阵模型。

为了利用穆勒矩阵模型对石英晶体的光学参数进行精确测量，我们将样品视为具有光学各向异性的均匀层，其介电常数$\varepsilon_j(j=1,2,3)$沿主轴方向独立，待拟合参数为介电常数ε_j、光学厚度d以及表征晶体光轴方位的欧拉角($\phi_{\mathrm{E}},\theta_{\mathrm{E}},\psi_{\mathrm{E}}$)。在反演待拟合参数的过程中，首先通过穆勒矩阵椭偏仪获取样品的穆勒矩阵测量值，然后通过穆勒矩阵模型进行迭代拟合。迭代拟合采用Levenberg-Marquardt算法[20-21]，通过非线性迭代回归来调整拟合参数使评价函数最小化，即当评价函数收敛到全局最小值时，则认为得到了样品的实际参数[22-23]。

评价函数用来评估所建模型的穆勒矩阵计算值与椭偏测量值之间的拟合效果，通常定义为均方根误差(RMSE,E_{RMS})，其表达式如下[24]：

$$E_{\mathrm{RMS}}=\frac{1}{\sqrt{16S-K}}\left[\sum_{j=1}^{s}\sum_{k=0}^{3}\sum_{l=0}^{3}\left(\frac{m_{kl,j}^{\exp}-m_{kl,j}^{\mathrm{cal}}}{\sigma_j}\right)^2\right]^{1/2},\tag{17}$$

式中：S和K分别表示数据点的个数和模型中待拟合参数的个数；下标k,l分别表示穆勒矩阵中元素的指标；上标exp和cal分别表示穆勒矩阵的测量值和计算值；σ_j表示与穆勒矩阵相关的测量误差。

迭代拟合后得到样品的主介电常数$\varepsilon_j(j=1,2,3)$后，可以由下式计算主折射率：

$$n_x^2=\varepsilon_1,\ n_y^2=\varepsilon_2。\tag{18}$$

再利用迭代拟合得到的样品厚度d，得出石英晶体波片的相位延迟量δ：

$$\delta=\frac{2\pi}{\lambda}|n_x-n_y|d,\tag{19}$$

式中：λ为入射光波长。

3 实验与讨论

实验中，使用双旋转补偿器型穆勒矩阵椭偏仪进行归一化穆勒矩阵的测量。该椭偏仪的测量光路如图2所示，主要包括光源、含起偏器和第一补偿器的偏振态产生模组(PSG)、真空吸附样品台、含第二补偿器和检偏器的偏振态分析模组(PSA)和探测器。该椭偏仪的测量波长范围为193～1690 nm，测量的重复性精度<0.005°，样品对准精度为0.001°，样品台转角精度为0.02°。该椭偏仪的偏振态产生模组和偏振态分析模组上均有旋转消色差补偿器，分别以不同角速度旋转，通过一次测量就可以得到样品的16个穆勒矩阵元素[25-29]。

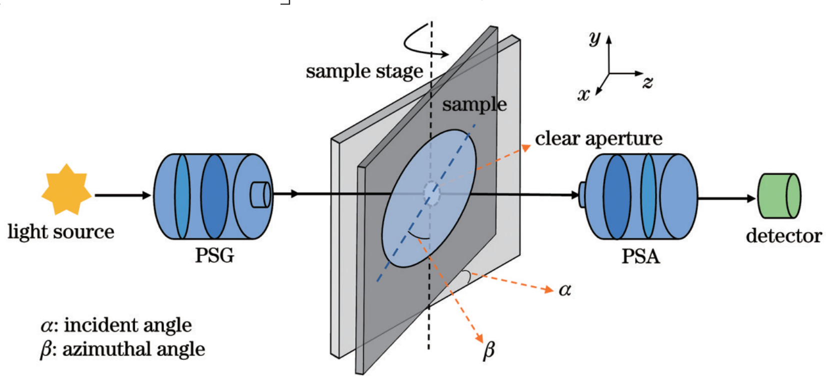

图2 测量系统示意图

Fig. 2 Schematic diagram of measuring system

对于石英晶体坐标系(a,b,c)，有三种切割方式。为了更好地验证本文所提出的穆勒矩阵模型的有效性，待测样品选用c切石英晶体，光轴方向垂直于样品表面，通过垂直于c轴、平行于a-b面切割得到。使用X射线晶体定向仪对样品的光轴方位进行测量，结果显示光轴偏移角为2′，表明样品的切割误差很小，可认为样品接近于标准c切石英晶体。

先对偏振态产生模组、偏振态分析模组进行高度和轴向校准，然后将样品吸附于椭偏仪样品台的通光孔上，选择透射测量模式。测量中保持偏振态产生模组、偏振态分析模组固定，绕y轴旋转样品台以改变入射光的角度α，在样品台平面内旋转样品以改变其放置方位角β。为了充分展现拟合模型的效果，我们测量了两种不同厚度的样品，两个样品均依次选择不同的方位进行放置，每个放置方位角下再选择不同的入射角进行测量。

样品平面垂直于入射光(即$\alpha=0°$)，样品的放置方位角依次被设置为0°、20°、40°、60°、80°、100°后采集透射椭偏数据，使用双旋转补偿器型穆勒矩阵椭偏仪内置模型对相位延迟量进行拟合，拟合结果如图3所示。在紫外波段，不同方位角下的相位延迟量的拟合结果均出现显著的非零值，最大值接近4°。理论上，垂直入

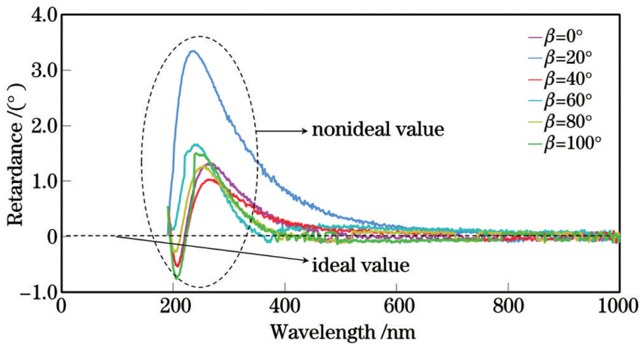

图3　不同方位角下使用内置模型拟合得到的相位延迟量色散曲线

Fig. 3　Phase retardation dispersion curves fitted with built-in model for different azimuthal angles

射c切石英晶体的光束对于任意的放置方位角测得的相位延迟量都应为零。显然，该内置模型对石英晶体相位延迟量的拟合存在缺陷，无法实现紫外波段c切石英晶体参数的准确测量。

在采用本论文所述穆勒矩阵模型进行实验的过程中，保持样品处于初始方位角即$\beta=0°$的位置，入射角α的变化范围为[0°，10°]，以2°为间隔测量穆勒矩阵数据并建立样品的穆勒矩阵模型。以厚样品为例，实际测量的穆勒矩阵元素色散曲线如图4(a)所示，利用穆勒矩阵模型拟合出的穆勒矩阵元素色散曲线如图4(b)所示，其中穆勒矩阵利用矩阵元m_{11}归一化。实际测量值与模型拟合值的差值曲线如图4(c)所示，

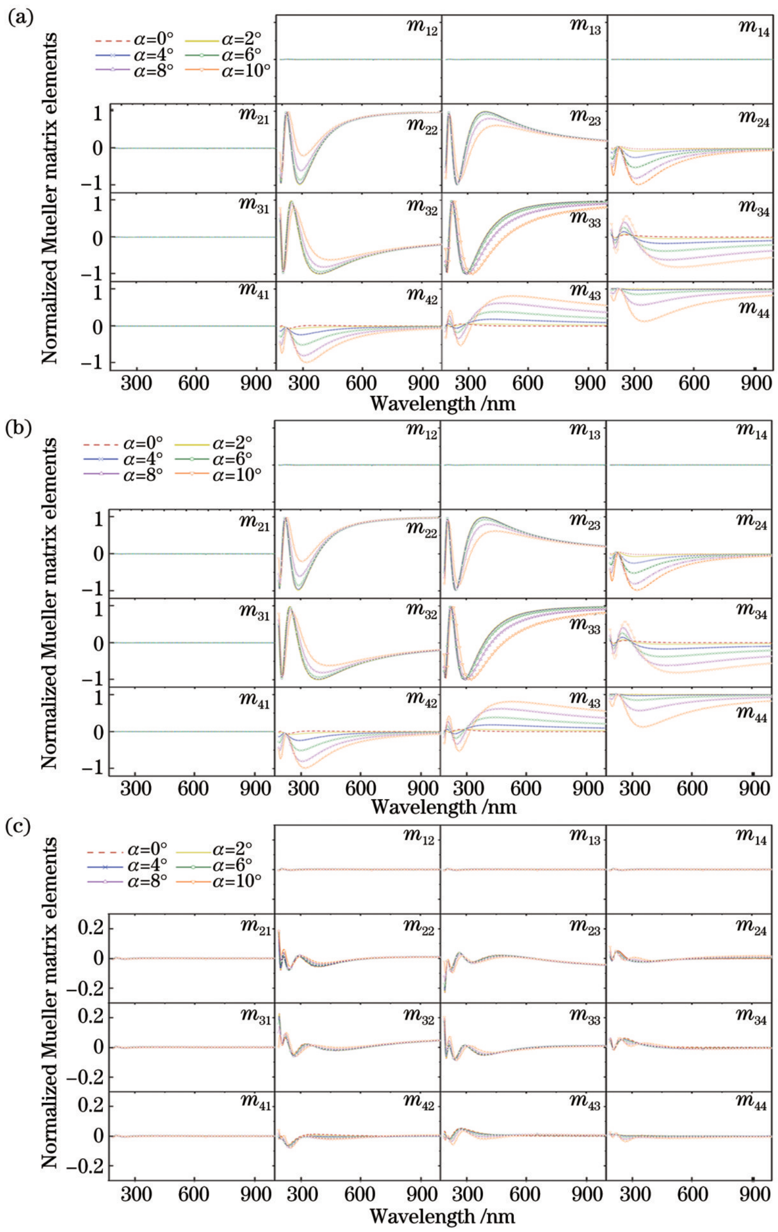

图4　厚样品的实际测量和拟合结果。(a)实际测量的穆勒矩阵元素色散曲线；(b)模型拟合的穆勒矩阵元素色散曲线；(c)实际测量值与模型拟合值的差值曲线

Fig. 4　Measurement and fitting results of thick sample. (a) Dispersion curves of actually measured Mueller matrix elements; (b) dispersion curves of Mueller matrix elements fitted by Mueller matrix model; (c) difference curves between actually measured values and model fitted values

差值的平均值为−0.0007,最大值为0.231。从穆勒矩阵元素的拟合结果可以看出,模型拟合曲线与实际测量曲线几乎完全重合,说明穆勒矩阵模型的拟合结果相当准确。

整个实验对厚、薄两种样品进行了测试,测试中在样品的方位角β依次为0°、45°、90°的情况下,入射角α在[0°,10°]范围内变化,变化步长仍然为2°,先后测量穆勒矩阵数据、建立穆勒矩阵模型。厚、薄两种样品在不同的放置方位角下,各个入射角的模型均方根误差结果如图5所示。厚样品均方根误差的最大值和平均值分别为4.182和4.127,薄样品均方根误差的最大值和平均值分别为3.906和3.770。较小的均方根误差值表明建立的穆勒矩阵模型对于不同的样品放置方位可以保持很好的稳定性,进一步验证了该模型的准确性。

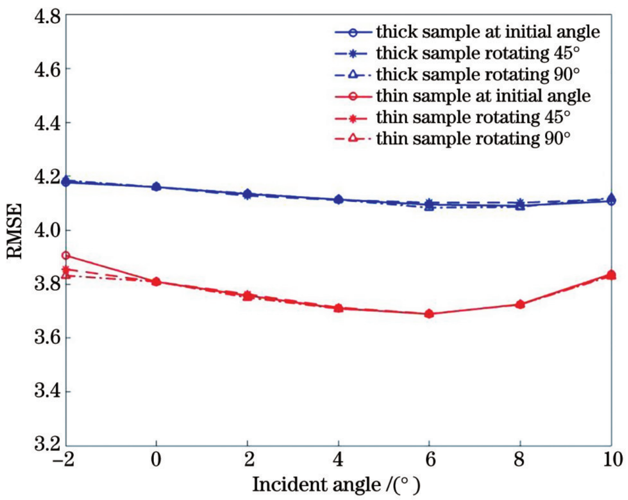

图5 厚、薄两种样品在不同的方位角和入射角下的均方根误差值

Fig. 5 RMSE values of two samples at different azimuthal angles and incident angles

穆勒矩阵模型中还包括了样品的厚度信息,从拟合结果可以获得样品的厚度d。采用千分尺(测量精度为0.01 mm)进行多次测量取均值的方法作为厚、薄两种样品的厚度参考值。厚、薄两种样品厚度的参考值和拟合值如表1所示,其相对误差分别为0.24%和0.57%。样品厚度的拟合值与参考值保持一致,更进一步地验证了穆勒矩阵模型的准确性。

表1 厚、薄两种样品的厚度

Table 1 Thicknesses of two samples unit: mm

Sample	Reference value	Fitting value
Thick quartz	0.834	0.832
Thin quartz	0.695	0.691

从穆勒矩阵模型的拟合结果中还可以获得晶体的双折射率,结合样品厚度d,代入式(19)即可计算出c切石英晶体在对应入射光波长下的相位延迟量。计算以193 nm波长为例,结果显示光束垂直入射c切石英晶体产生了微小相位延迟量。由模型的拟合结果还能得到欧拉角θ_E,θ_E表征的是c切石英晶体的c轴与测量坐标系中z轴的夹角,该欧拉角的存在验证了晶体光轴与测量坐标系方向的不一致。两种厚度的样品的相位延迟量和欧拉角参数如表2所示。欧拉角的拟合结果与X射线晶体定向仪的测量值(2′)相吻合,更充分地证明了该模型的准确性。

表2 两种样品的拟合参数结果

Table 2 Fitting parameter results of two samples

Sample	Phase retardation at 193 nm /(°)	Euler angle θ_E /(′)
Thick quartz	1.71	1.902
Thin quartz	0.77	1.932

4 结 论

本文提出了一种精确测量石英晶体参数的穆勒矩阵模型。基于坐标变换和Berreman 4×4矩阵理论,建立起穆勒矩阵测量值与晶体厚度、欧拉角和介电张量的关联模型,并采用均方根误差作为标准来评价模型的拟合效果。实验结果显示,穆勒矩阵元素的实际测量色散曲线与模型拟合的色散曲线高度一致。在不同的样品方位角和入射角下模型的均方根误差值都能稳定在较小的范围内:厚样品均方根误差的最大值和平均值分别为4.182和4.127,薄样品均方根误差的最大值和平均值分别为3.906和3.770。拟合得到的厚度与千分尺测量结果相近:厚、薄两种样品的拟合厚度分别为0.832 mm和0.691 mm,千分尺的测量厚度分别为0.834 mm和0.695 mm,相对误差分别为0.24%和0.57%。拟合得到的欧拉角θ_E分别为1.902′和1.932′,与X射线晶体定向仪的测量结果吻合。实验结果充分表明建立的穆勒矩阵模型拟合结果的准确性,并成功得到了石英晶体的厚度、欧拉角和相位延迟量。利用本模型结合双旋转补偿器型穆勒矩阵椭偏仪,通过简单的测量步骤和模型拟合即可精准地得到样品的丰富信息,为精确测量各向异性材料的参数提供了重要的参考。

参 考 文 献

[1] Jousset P, Reinsch T, Ryberg T, et al. Dynamic strain determination using fibre-optic cables allows imaging of seismological and structural features[J]. Nature Communications, 2018, 9(1): 1-11.

[2] Gu N T, Xiao Y W, Huang L H, et al. Polarization imaging based on time-integration by a continuous rotating polarizer[J]. Optics Express, 2022, 30(3): 3497-3515.

[3] Liu T C, Lin L P, Bi X X, et al. *In situ* quantification of interphasial chemistry in Li-ion battery[J]. Nature Nanotechnology, 2019, 14(1): 50-56.

[4] Xu Z J, Dong Y, Tseng C K, et al. CMOS-compatible all-Si

metasurface polarizing bandpass filters on 12-inch wafers[J]. Optics Express, 2019, 27(18): 26060-26069.

[5] Zheng S Q, Lin Q G, Cai Y, et al. Improved common-path spectral interferometer for single-shot terahertz detection[J]. Photonics Research, 2018, 6(3): 177-181.

[6] 唐凡春, 步扬, 吴芳, 等. 基于径向偏振光的波片参数测量方法[J]. 中国激光, 2022, 49(17): 1704006.
Tang F C, Bu Y, Wu F, et al. Parameter measurement of wave plate based on radially polarized beams[J]. Chinese Journal of Lasers, 2022, 49(17): 1704006.

[7] Liu W X, Liu M, Zhang S L. Method for the measurement of phase retardation of any wave plate with high precision[J]. Applied Optics, 2008, 47(30): 5562-5569.

[8] Chen K H, Lin C H, Liu P C. An interferometric method for simultaneously determination the phase retardation and fast-axis azimuth angle of a wave plate[J]. Journal of Modern Optics, 2020, 67(11): 992-997.

[9] 陈强华, 关裕, 周胜, 等. 基于双频激光干涉相位检测的高精度波片测量[J]. 光学学报, 2023, 43(1): 0112002.
Chen Q H, Guan Y, Zhou S, et al. High-accuracy wave plate measurement based on dual-frequency laser interferometry and phase detection[J]. Acta Optica Sinica, 2023, 43(1): 0112002.

[10] Zeng A J, Li F Y, Zhu L L, et al. Simultaneous measurement of retardance and fast axis angle of a quarter-wave plate using one photoelastic modulator[J]. Applied Optics, 2011, 50(22): 4347-4352.

[11] Williams P A, Rose A H, Wang C M. Rotating-polarizer polarimeter for accurate retardance measurement[J]. Applied Optics, 1997, 36(25): 6466-6472.

[12] Gu H G, Chen X G, Shi Y T, et al. Comprehensive characterization of a general composite waveplate by spectroscopic Mueller matrix polarimetry[J]. Optics Express, 2018, 26(19): 25408-25425.

[13] Gu H G, Chen X G, Zhang C W, et al. Study of the retardance of a birefringent waveplate at tilt incidence by Mueller matrix ellipsometer[J]. Journal of Optics, 2018, 20(1): 015401.

[14] Berreman D W. Optics in stratified and anisotropic media: 4×4-matrix formulation[J]. Journal of the Optical Society of America, 1972, 62(4): 502-510.

[15] Schubert M. Polarization-dependent optical parameters of arbitrarily anisotropic homogeneous layered systems[J]. Physical Review B, 1996, 53(8): 4265-4274.

[16] Grundmann M, Sturm C, Kranert C, et al. Optically anisotropic media: new approaches to the dielectric function, singular axes, microcavity modes and Raman scattering intensities[J]. Physica Status Solidi (RRL) Rapid Research Letters, 2017, 11(1): 1600295.

[17] Fujiwara H. Spectroscopic ellipsometry: principles and applications[M]. Singapore: Wiley, 2007.

[18] Azzam R M A, Bashara N M, Ballard S S. Ellipsometry and polarized light[J]. Physics Today, 1978, 31(11): 72.

[19] Jellison G E, Jr. Spectroscopic ellipsometry data analysis: measured versus calculated quantities[J]. Thin Solid Films, 1998, 313/314: 33-39.

[20] Zhang S, Jiang H, Gu H G, et al. High-speed Mueller matrix ellipsometer with microsecond temporal resolution[J]. Optics Express, 2020, 28(8): 10873-10887.

[21] Arwin H, Berlind T, Johs B, et al. Cuticle structure of the scarab beetle *Cetonia aurata* analyzed by regression analysis of Mueller-matrix ellipsometric data[J]. Optics Express, 2013, 21(19): 22645-22656.

[22] Ge B L, Larson S, Tu H T, et al. Generalized ellipsometry characterization of Ag nanorod arrays prepared by oblique angle deposition[J]. Nanotechnology, 2020, 31(7): 075705.

[23] Shan Y, Liu P, Chen Y, et al. Microstructure-induced anisotropic optical properties of YF_3 columnar thin films prepared by glancing angle deposition[J]. Nanomaterials, 2020, 10(12): 2413.

[24] Losurdo M, Hingerl K. Ellipsometry at the nanoscale[M]. Berlin: Springer, 2013.

[25] Li J, Ramanujam B, Collins R W. Dual rotating compensator ellipsometry: theory and simulations[J]. Thin Solid Films, 2011, 519(9): 2725-2729.

[26] 范真涛. 穆勒矩阵椭偏测量系统高级参数问题研究[D]. 成都: 中国科学院光电技术研究所, 2019: 13-17.
Fan Z T. Research on the advanced parameters problem of Mueller matrix ellipsometry system[D]. Chengdu: Institute of Optics and Electronics, Chinese Academy of Sciences, 2019: 13-17.

[27] Hilfiker J N, Hong N N, Schoeche S. Mueller matrix spectroscopic ellipsometry[J]. Advanced Optical Technologies, 2022, 11(3/4): 59-91.

[28] Chen X G, Gu H G, Liu J M, et al. Advanced Mueller matrix ellipsometry: instrumentation and emerging applications[J]. Science China Technological Sciences, 2022, 65(9): 2007-2030.

[29] 郑州, 侯俊峰. 单波长中红外穆勒矩阵椭偏仪的设计、定标与测试[J]. 光学学报, 2022, 42(18): 1812004.
Zheng Z, Hou J F. Design, calibration, and measurement of single wavelength mid-infrared Mueller matrix ellipsometer[J]. Acta Optica Sinica, 2022, 42(18): 1812004.

Mueller Matrix Model in Ellipsometry Measurement of Quartz Crystal

Zhao Yu[1,2], Zhang Linghao[1,2], Zeng Aijun[1,2*], Huang Huijie[2], Avakaw Sergey[3]

[1]*Laboratory of Information Optics and Optoelectronic Technology, Shanghai Institute of Optics and Fine Mechanics, Chinese Academy of Sciences, Shanghai* 201800, *China*;

[2]*Center of Materials Science and Optoelectronics Engineering, University of Chinese Academy of Sciences, Beijing* 100049, *China*;

[3]*Company of KBTEM-OMO Republication Unitary Scientific and Production Enterprise, Minsk* 220033, *Belarus*

Abstract

Objective Quartz crystal is an important birefringence material, which is widely used in optical related fields. The two main optical parameters of quartz crystal wave plate are phase retardation and fast axis azimuth. Due to the influence of manufacturing process, these two actual parameters will deviate from the theoretical value, so it is usually necessary to accurately measure the optical parameters before use. Ellipsometry is usually used to measure the parameters of quartz crystal in a wide spectrum, but the existing ellipsometric measuring instruments often assume that the optical axis of the crystal is aligned with the measuring optical path, which introduces measurement error, especially in the ultraviolet band. Therefore, it is necessary to propose a fitting model for accurate measurement of quartz crystal parameters. The model contains rich information and the fitting results are accurate. This model has important reference value for measuring the accurate parameters of anisotropic materials by ellipsometry.

Methods A Mueller matrix model for accurate measurement of quartz crystal parameters by ellipsometry is proposed. Firstly, the crystal coordinate system (a, b, c) is transformed into the measurement coordinate system (x, y, z) by coordinate transformation, which involves three Euler angles ϕ_E, θ_E, and ψ_E (Fig. 1). After coordinate transformation, the expression of dielectric tensor of quartz crystal in the measurement coordinate system can be obtained. Then, the Berreman 4×4 matrix theory is used to establish the correlation between quartz crystal parameters and Mueller matrix. The Mueller matrix measurement value of the sample is obtained by the Mueller matrix ellipsometer, and then the Mueller matrix model is used for iterative fitting. The Levenberg-Marquardt algorithm is used for fitting, and the evaluation function is defined as root mean square error (RMSE). The fitting parameters are adjusted by nonlinear iterative regression to minimize the evaluation function, that is, when the evaluation function converges to the global minimum, the actual parameters of the sample are obtained. Finally, the thickness of the crystal, Euler angles and the phase retardation can be obtained by fitting calculation.

Results and Discussions In order to fully demonstrate the effect of the fitting model, we measured two samples with different thicknesses. Both samples were placed in different directions in turn, and different incident angles were selected for measurement at each placement azimuth (Fig. 2). Firstly, the built-in model of ellipsometer is used to fit the phase retardation. In the ultraviolet band, the fitting results of the phase retardation at different azimuth angles show significant non-zero values, and the maximum value is close to 4° (Fig. 3). Obviously, the built-in model has defects in fitting the phase retardation of quartz crystal. The Mueller matrix model described in this paper is then used for experiments. Taking the thick sample as an example, the actual measured Mueller matrix dispersion curve [Fig. 4(a)], the Mueller matrix dispersion curve fitted by the Mueller matrix model [Fig. 4(b)], and the difference between the two curves [Fig. 4(c)] can be obtained. The average value of the difference is −0.0007, and the maximum value is 0.231. At different sample azimuth angles and incident angles, the maximum and average RMSE of thick samples are 4.182 and 4.127, respectively, and the maximum and average RMSE of thin samples are 3.906 and 3.770, respectively (Fig. 5). The fitting thicknesses of thick and thin samples are 0.832 mm and 0.691 mm, respectively. In comparison, the measured thicknesses using micrometers are 0.834 mm and 0.695 mm, respectively. The relative errors are 0.24% and 0.57%, respectively (Table 1). The Euler angles θ_E of thick and thin samples are 1.902′ and 1.932′, respectively.

Conclusions This paper proposes a Mueller matrix model for accurately measuring quartz crystal parameters. Based on the coordinate transformation and Berreman 4×4 matrix theory, the correlation model between the measured values of Mueller matrix and crystal thickness, Euler angle and dielectric tensor is established, and the fitting effect of the model is evaluated by using the RMSE as the evaluation function. The experimental results show that the fitted Mueller matrix dispersion curves are highly consistent with the measured dispersion curves. The RMSE of the model can be stabilized in a small range (<5) under different sample azimuth angles and incident angles. The thickness obtained by fitting is similar to that measured by micrometer (relative error <1%), and the fitted Euler angle is consistent with the measurement results. The experimental results fully show the accuracy of the fitting results of the established Mueller matrix model, and the thickness, Euler angle and phase retardation of the quartz crystal are successfully obtained. Using this model combined with the dual-rotating compensator Mueller matrix ellipsometer, rich information of the sample can be accurately obtained through simple measurement steps and model fitting, which provides an important reference for accurately measuring the parameters of anisotropic materials.

Key words measurement; ellipsometry; quartz crystal; dielectric tensor; phase retardation; Euler angle